Simultaneous observations of tropospheric turbulence from radiosondes using Thorpe analysis and the VHF MU radar

Hubert Luce, Richard Wilson, Francis Dalaudier, Hiroyuki Hashiguchi, Noriyuki Nishi, Yoshiaki Shibagaki, Tomoyuki Nakajo

AGU PUBLICATIONS

Radio Science

RESEARCH ARTICLE
10.1002/2013RS005355

Key Points:
- Simultaneous observations of turbulence from radar and balloon techniques
- Original comparisons of turbulence from radar and radiosondes
- Signature of turbulence in VHF radar echoes and temperature profiles

Correspondence to:
H. Luce,
luce@univ-tln.fr

Citation:
Luce, H., R. Wilson, F. Dalaudier, H. Hashiguchi, N. Nishi, Y. Shibagaki, and T. Nakajo (2014), Simultaneous observations of tropospheric turbulence from radiosondes using Thorpe analysis and the VHF MU radar, *Radio Sci.*, *49*, 1106–1123, doi:10.1002/2013RS005355.

Received 12 DEC 2013
Accepted 25 SEP 2014
Accepted article online 30 SEP 2014
Published online 21 NOV 2014

Simultaneous observations of tropospheric turbulence from radiosondes using Thorpe analysis and the VHF MU radar

H. Luce[1], R. Wilson[2], F. Dalaudier[2], H. Hashiguchi[3], N. Nishi[4], Y. Shibagaki[5], and T. Nakajo[6]

[1]Université de Toulon, CNRS/INSU, IRD, Mediterranean Institute of Oceanography, Toulon, France, [2]Université Pierre et Marie Curie, CNRS/INSU, LATMOS-IPSL, Paris, France, [3]Research Institute for Sustainable Humanosphere, Kyoto University, Kyoto, Japan, [4]Department of Earth System Science, Faculty of Science, Fukuoka University, Fukuoka, Japan, [5]Department of Electrical, Electronics and Computer Engineering, Osaka Electro-Communication University, Neyagawa, Japan, [6]Department of Telecommunications and Computer Networks, Fukui University of Technology, Fukui, Japan

Abstract This paper deals with the detection and quantification of refractivity turbulence in the troposphere from radiosonde and very high frequency (VHF) band radar data. Balloon data processing methods based on Thorpe sorting and recently developed by Wilson et al. (2010, 2011, and 2013) can be applied for a direct identification of turbulent layers from the in situ profiles. The VHF band mid and upper atmosphere radar (MUR) can be operated in range-imaging mode for detecting and monitoring turbulent layers at high time and range resolutions (of the order of 10 s and a few tens of meters, respectively). For cross validating the techniques, concurrent MUR and RS92-SGP Vaisala radiosonde observations were made at the Shigaraki Middle and Upper atmosphere (MU) observatory (34.85°N, 136.15°E; Japan) during a field campaign of 3 weeks in September 2011. The radar signature, in terms of echo power and aspect ratio, of the turbulent layers identified from balloon data analyses is investigated from case studies and statistics. The deep ($>$ ~100 m) layers are very often associated with echo power maxima and weak aspect ratios suggesting that the same events of isotropic turbulence were detected by both instruments. Some others are associated with relative minima of isotropic echo power, possibly indicating a later stage of turbulence. The ranges of strong aspect ratios are generally not associated with turbulent events in the balloon data supporting the hypothesis that anisotropic turbulence is not the cause of vertically enhanced radar echoes. Quantitative comparisons are made between radar echo power and refractive index constant structure C_n^2 estimated from temperature variance and additional parameters in the selected layers. Despite a large scatter between the radar and balloon estimates, the results are statistically significant (correlation coefficients ~0.5–0.88) even when the causes of systematic decrease with height of C_n^2 (humidity and density) are removed. Our studies therefore demonstrate that radar and balloon observations of turbulence are consistent between each other and that new insights on tropospheric turbulence can be obtained by the two techniques as stand-alone systems.

1. Introduction

Small-scale turbulence can have an impact on the mixing of passive tracers, the life cycle of clouds, larger scale dynamics (e.g., waves, general circulation of the atmosphere through dissipation of kinetic energy), local stratification through diffusion, and human activities (telecommunications, remote sensing, and air transport). Turbulence in the troposphere can be generated by various instabilities resulting from wind shears, wave breaking, nonlinear wave-wave interaction, thermal convection, latent heat release, and radiative effects. These mechanisms can interact between each other giving rise to miscellaneous characteristics of the turbulent regions from highly sporadic patches to long-lived layers with strongly varying depth and intensity.

Experimental studies on atmospheric turbulence can be made from balloon and radar observations. Commonly used balloon-borne radiosondes now provide measurements of pressure, temperature, humidity, and horizontal winds along the balloon path at a time resolution of ~1 s. Such a high resolution enables the identification of unstable regions (or overturns) locally produced by turbulent stirring and instabilities into potential temperature profiles. The identification method is based on Thorpe sorting of the potential density profiles [*Thorpe*, 1977] and the practical application to atmospheric data was recently refined by *Wilson et al.* [2010, 2011] through the development of objective and robust methods for rejecting artificial overturns produced by noise. In addition, VHF band stratosphere-troposphere (ST) radars can provide information on

atmospheric turbulence through the measurements of received power and width of the Doppler spectrum. Indeed, ST radar echoes are partly due to Bragg scatter from humidity and temperature irregularities caused by turbulence in both clear air and cloudy conditions [e.g., *Röttger*, 1980]. Depending on their size, these irregularities can be nearly isotropic if turbulence is weakly affected by the environmental stability of the stratification or can be strongly anisotropic otherwise. Anisotropic turbulence at the Bragg scale (~3 m for VHF band radars) can potentially produce enhanced echoes at vertical incidence with respect to off-vertical directions. The vertically enhanced echoes are said to be "aspect sensitive." The humidity and temperature irregularities can also be nearly one-dimensional along the vertical and can take the form of stable gradient sheets. Partial reflection from stable gradient sheets is also a widely accepted mechanism for explaining aspect sensitivity [e.g., *Röttger and Liu*, 1978; *Luce et al*., 1995].

Concurrent measurements with the VHF band mid and upper atmosphere radar (MUR) and 59 RS92-SGP radiosondes were performed at the Shigaraki MU Observatory on 5–26 September 2011. MUR was continuously operated in range-imaging mode [e.g., *Luce et al*., 2006] in order to retrieve power profiles at a range sampling of 5 m and a time resolution of ~12 s. Thirty-six radiosondes were launched during night period (and thus 23 during daytime). The balloons were slightly under inflated in order to increase the vertical resolution of the measurements by reducing their speed ascent. In addition, the raw balloon data sampled at a rate of 1 Hz were used. It follows that profiles at a vertical resolution of 3–6 m could be obtained, instead of ~10 m for standard soundings. The data collected during daytime were not used because of contamination due to the solar heating of the sensors.

The present study is thus aimed at using radar and balloon data at unprecedented resolutions for detecting and monitoring refractivity turbulence in the troposphere. Refractivity turbulence structure constants C_n^2 estimated from balloon data within the selected layers were compared with the averaged values of radar echo power measured in the altitude range of the layers. Comparing turbulence statistics retrieved from radar and balloon data needs the hypothesis that the statistical properties of the turbulent irregularities are identical in the radar volume and along the balloon path despite the balloon drift, up to a horizontal distance from the launching site of 100 km typically at the tropopause during autumn jet stream conditions. We assume that comparisons of statistics are justified if the turbulent layers, found to be detected by the two instruments, are generated by the same source.

After a brief description of the methods used for analyzing the radar and balloon data in section 2, the results of comparisons are presented in section 3. The conclusions of this work are given in section 4.

2. Data and Processing

2.1. Balloon Data

2.1.1. Principle of Overturn Detection

The detection of overturning regions from balloon data is based on the Thorpe sorting of vertical profiles of conserved variables under dry conservative or moist conservative adiabatic processes [*Wilson et al*., 2013, hereafter noted W13]. The Thorpe sorting is applied to a potential temperature θ^*, which results from the numerical integration of the Brünt-Vaïsälä frequency N, which takes its "dry" expression (i.e., $N^2 = g\ \mathrm{d}\ln\theta/\mathrm{d}z$, where θ is the dry potential temperature and g is the acceleration of gravity) for nonsaturated air and a "moist" expression for saturated air [e.g., *Lalas and Einaudi*, 1974; *Durran and Klemp*, 1982; *Emanuel*, 1994]. This procedure allowed a successful detection of turbulence in clouds [W13].

Turbulent stirring or convective instabilities giving rise to turbulent motions at high Reynolds numbers produce local overturns (i.e., dry or moist superadiabatic lapse rates). The difference between the measured and sorted profiles would make it possible to detect these overturns [e.g., *Thorpe*, 1977]. However, instrumental noise can have a tremendous effect by generating artificial overturns. *Wilson et al*. [2010, 2011] proposed an objective and robust method based on an optimal filtering and a statistical test for rejecting these artificial overturns with a given statistical confidence. The minimum detectable depth of the overturns primarily depends on both the instrumental noise level and the background stability of the stratification.

The Vaisala software delivers raw profiles of temperature, relative humidity with respect to liquid condensation, pressure, and zonal and meridional winds at the vertical sampling rate of 1 Hz so that temperature profiles can be retrieved at a vertical resolution of ~3–6 m depending on the ascent speed of the

balloons. Because the processing method of the raw data is described in detail by *Wilson et al*. [2011], the main steps are only briefly described here. The effects of quantization noise of the pressure measurements made at a resolution of 10 Pa is important. Consequently, the measured series of pressure is not strictly a decreasing monotonic profile. To work around this issue, the pressure profile is first interpolated with a least square cubic spline approximation before estimating the altitude using the hydrostatic equilibrium equation. The profiles of temperature, pressure, and humidity are then resampled by linear interpolation at a regular vertical step. The vertical sampling is an integer value close to the median of the measured (variable) vertical step. The dry conservative and moist conservative potential temperature profiles are inferred from the resampled profiles (see section 2.1.2).

The selection method requires the knowledge of the noise level of the potential temperatures. The instrumental noise level of the temperature, pressure, and humidity is first estimated from the raw data. The noise level on θ, found to be altitude dependent, is then deduced. The noise level on moist θ is supposed to be nearly equal.

A statistical hypothesis test allows the rejection of artificial (i.e., noise-induced) overturns. Before applying the test, smoothing and undersampling are performed in order that the first differences in the potential temperature profile are, in the average, significantly larger than the noise level [see *Wilson et al*., 2010 for more details].

2.1.2. Potential Temperature Profiles

The principle of calculation of the potential temperatures was described in W13. We just briefly recall the fundamentals. For a subsaturated atmosphere, the potential temperature θ_0 (K) at the altitude z_0 is estimated from the relation

$$\theta_0 = \theta(z_0) = T_0\left(\frac{1000}{p_0}\right)^{2/7} \tag{1}$$

where T_0 is temperature (K) and p_0 is pressure (hPa) at z_0. The paramenter θ_{i+1} at $z_i + \Delta z$ is given by

$$\theta_{k+1} = \theta_k\left(1 + N^2\frac{\Delta z}{g}\right) \tag{2}$$

For a moist saturated air, N^2 was replaced by an expression valid for moist air [W13].

Using the same balloon data set as in the present study, W13 showed that the proportion of the troposphere found to be turbulent can dramatically increase if saturation effects are taken into account. Indeed, static stability is always smaller in saturated regions than in dry regions so that dynamic or convective instabilities, and then turbulence, can more easily be generated. This result is also consistent with the fact that clouds are generally turbulent [e.g., *Houze*, 1993]. In W13, the saturated regions were selected from the relative humidity profiles using empirical criteria proposed by *Zhang et al*. [2010] specifically dedicated to RS92SGP Vaisala radiosondes. The results of comparisons between radar and balloon data presented here will thus be based on those obtained by W13 including saturation effects.

2.1.3. Estimates of C_n^2 From In Situ Measurements

Local superadiabatic lapse rates are not necessarily a direct signature of stirring from turbulence. For example, the rolling up of stable density surfaces at the initial stage of Kelvin-Helmholtz instability is a typical process which can give rise to overturns before possibly breaking into 3-D turbulence. Therefore, the estimates of turbulence statistics from the sole detection of overturns from balloon data, i.e., without additional information from other instruments, should be, in principle, treated with caution. The interpretation (in a statistical sense) of the overturning regions as structures resulting from turbulent mixing processes will be confirmed a posteriori from comparisons with radar data.

We first estimated the temperature structure constant C_T^2, which is a measure of the temperature fluctuation intensity for stationary, locally homogeneous, and isotropic turbulence in the inertial subrange. There are different methods for estimating C_T^2 from temperature profiles collected from a single sensor. C_T^2 can be estimated from the calculation of temperature spectra and temperature structure functions. However, these methods do not provide accurate results for short samples (as is often the case here due to the shallow depth of most layers) and, thus, were not used here. We rather used a method that relates the temperature variance σ_T^2 to the level of the temperature spectrum within the inertial subrange. In practice, σ_T^2 is simply the unbiased variance of temperature fluctuations obtained by subtracting a linear trend to the observed temperature profile over the depth of the selected layer. There is therefore a single estimate of σ_T^2 for each selected layer.

The 1-D Kolmogorov-Obukhov-Corrsin temperature spectrum $S_T(k)$ has a universal shape and is given by $S_T(k) = 0.25C_T^2 k^{-5/3}$ between the inner scale l_i and a cutoff scale L_c (defined later). For scales larger than L_c, the turbulence properties are not universal, and for the sake of simplicity, a white spectrum is assumed. In addition, it is assumed that $L_c \gg l_i$, which is a necessary condition for the existence of an inertial domain. The variance σ_T^2 is thus related to the temperature spectra by

$$\sigma_T^2 = \int_0^{k_c} S_W(k)\mathrm{d}k + \int_{k_c}^{k_i} S_T(k)\mathrm{d}k \tag{3}$$

where $S_W(k) = 0.25C_T^2 k_c^{-5/3}$ is the white spectrum and k_c and k_i are the wave numbers corresponding to L_c and l_i, respectively. The integration of (3) with the condition $k_c \ll k_i$ gives the following:

$$C_T^2 = \frac{8}{5}\sigma_T^2 k_c^{2/3} \tag{4a}$$

Any other realistic spectrum for $k < k_c$ would produce a relation close to (4a), i.e.,

$$C_T^2 = a\frac{8}{5}\sigma_T^2 k_c^{2/3} \tag{4b}$$

where a is of the order of *unity*.

For stratified turbulence, the cutoff wave number k_c should be related to an outer scale of turbulence such as the buoyancy or the Ozmidov scale. Various studies [*Dillon*, 1982; *Smyth et al.*, 2001] suggested that the Thorpe scale defined as $L_T = \langle l^2 \rangle_h^{1/2}$ (where l are the vertical displacements and $< >_h$ is the average over the depth h of the layer) is closely related to these scales for fully developed turbulence, i.e., $k_c \propto 1/L_T$. For our purpose, it is enough to assume that $k_c = 1/L_T$. Because any other choice would modify the constant parameter a only, it does not affect the comparisons between C_n^2 and radar echo power made in relative levels. Therefore, we obtain

$$C_T^2 = a\frac{8}{5}\sigma_T^2 L_T^{-2/3} \tag{5}$$

Then, the structure constant C_n^2 for dry air, which is a measure of refractivity turbulence, is deduced from [*Tatarski*, 1961]

$$C_n^2[\mathrm{dry}] = \left(\frac{0.776\times 10^{-6} p}{T^2}\right)^2 C_T^2 \tag{6a}$$

where p is pressure (Pa) and T is temperature (K). C_n^2 for moist but nonsaturated air is given by [e.g., *Luce et al.*, 1996]:

$$C_n^2[\mathrm{moist}] = \left(\frac{M_h^2}{M_d^2}\right) C_n^2[\mathrm{dry}] \tag{6b}$$

where M_d and M_h are the dry and humid vertical gradient of potential refractive index. They are given by

$$M_h = -0.776 \times 10^{-6}\frac{P}{T^2}\left(1 + 15600\frac{q}{T}\right)\left(\frac{\mathrm{d}T}{\mathrm{d}z} + \Gamma_a - \frac{7800}{1 + 15600q/T}\frac{\mathrm{d}q}{\mathrm{d}z}\right) \tag{7}$$

and

$$M_d = -0.776 \times 10^{-6}\frac{p}{T^2}\left(\frac{\mathrm{d}T}{\mathrm{d}z} + \Gamma_a\right), \tag{8}$$

respectively. The paramenter q is the specific humidity (g/g) and $\Gamma_a = -9.8 \times 10^{-3}$ K m^{-1} is the dry adiabatic lapse rate.

For a saturated air, M_h should be replaced by a saturated potential refractive index gradient M_s. An expression of M_s was proposed by *Vaughan and Worthington* [2000, their expression (15)] following the approach given by *Ottersten* [1969] for a subsaturated air. It assumes displacements of air parcels along the moist adiabatic lapse rate rather than the dry adiabatic. This model is a limit case where partial pressure of humidity instantaneously equilibrates with temperature fluctuations and assumes no heat diffusion between condensed particles and air. Because M_s can tend to zero for some cases, the use of M_s can yield a strong underestimate of C_n^2 for some saturated layers. We found that this is the case in the height range 7–11 km where the sign of M_s changes and thus where M_s passes through zero (see Appendix A). Consequently, even if the

expression for unsaturated air (7) should produce slight overestimates for nearly saturated and saturated airs and to slight underestimates for dry air according to *Vaughan and Worthington* [2000], it was used for the comparisons for all the selected layers. To the authors' knowledge, such a problem was not addressed in any previous paper—except in *Vaughan and Worthington* [2000]—describing comparison results between profiles of the power of radar echoes received at vertical incidence and M^2, the latter parameter being always estimated for a nonsaturated atmosphere. Despite this, the comparison results were always considered as relatively good, at least in a statistical sense, at a range resolution of 150 m [e.g., *Tsuda et al*., 1988; *May et al*., 1991].

2.2. Radar Data

2.2.1. Radar Data Processing

MUR is a Doppler-pulsed radar operating at 46.5 MHz (6.45 m radar wavelength, 3.5 MHz bandwidth, and 1 MW peak output power) [e.g., *Fukao et al*., 1990]. The radar can be operated in range-imaging mode using frequency diversity, also called FII technique by *Luce et al*. [2001]. The technique consists in transmitting several closely spaced frequencies switched pulse to pulse. The collected data at the various frequencies are processed using the adaptive Capon processing method. During the campaign, the radar was operated with five frequencies from 46.0 MHz to 47.0 MHz with a constant frequency spacing of 0.25 MHz. The radar antenna beam was steered into three directions (one vertical and two oblique directions at 10° off zenith toward North, East). The number of coherent integrations was set equal to 32. The acquisition time of the time series for retrieving a vertical profile was ~24 s, but the effective time resolution was ~12 s due to Hanning windowing of the time series before fast Fourier transform. In addition, data processing was performed every ~6 s for a better time continuity. A 16 bit optimal code was used for the transmitted pulse. The subpulse duration was 1 μs. This duration corresponds to a range resolution of 150 m before application of the range-imaging technique. In range-imaging mode, the vertical sampling was arbitrarily set to 5 m (this is not the range resolution, since it depends on SNR) from the altitudes of 1.245 km to 20.445 km above sea level (asl). The output of the Capon filter is the "Capon power." It is the sum of the atmospheric signal and noise powers. For each vertical profile, a value of the noise power was estimated from Doppler spectra calculated at altitudes where atmospheric echoes were negligible in order to avoid possible contamination of the noise power from atmospheric signals. This value (in dB) was subtracted from each point of the Capon power (dB) profile to get the power profile (in dB, relative units) used in the present study.

2.2.2. Reconstruction of Mean Profiles of Echo Power

Among other difficulties inherent in the comparison between radar and balloon data, a single radar profile acquired in a few tens of seconds or even in a few seconds is very likely not representative of instantaneous measurements made by radiosondes along the balloon path for the time necessary for the balloons to reach the tropopause, i.e., ~1 h. The statistical representativeness of the structures detected by radar can be improved in some way by time averaging. It is usual to average the radar profiles over a period corresponding to the balloon flight time [e.g., *Tsuda et al*., 1988]. Therefore, a first set of radar profiles used for the comparisons were obtained by averaging radar profiles collected for 60 min after the balloon launches. Such a time averaging can, however, smooth out more sporadic but intense events. We propose to use a second set of radar profiles built as follows. As shown by *Luce et al*. [2007], who compared N^2 profiles from radar and balloon data at stratospheric heights at a vertical resolution of 50 m, taking account for the advection of the air parcels by the horizontal wind may improve the results of comparisons if the turbulent irregularities can be considered as frozenly advected. The positive or negative time lag Δt for which the air parcels met by the balloons that passed closest to the radar was estimated at the height of the vertical sampling of the radar profiles. We thus selected the radar data around the time t of the balloon measurements minus the time lag Δt (i.e., around the time $t' = t - \Delta t$). We finally constructed composite profiles of the radar echo power by averaging the radar profiles in the range $t' \pm \delta/2$ where δ was set to 2 to 60 min in order to study the effects of time averaging (see example Figure 4 for $\delta = 10$ min). Arbitrarily, $\delta = 10$ min was the time-averaging reference for some results presented here. As we shall see, statistical results do not significantly differ when using composite profiles averaged over 10 min rather than the 60 min averaged profiles.

3. Results

3.1. Balloon Data

Figure 1a shows the mean ascent speed of the 36 balloons (top panel), the tropical (thermal) tropopause height (middle panel) and the horizontal distance between the balloons and MUR at the tropopause height, i.e., the

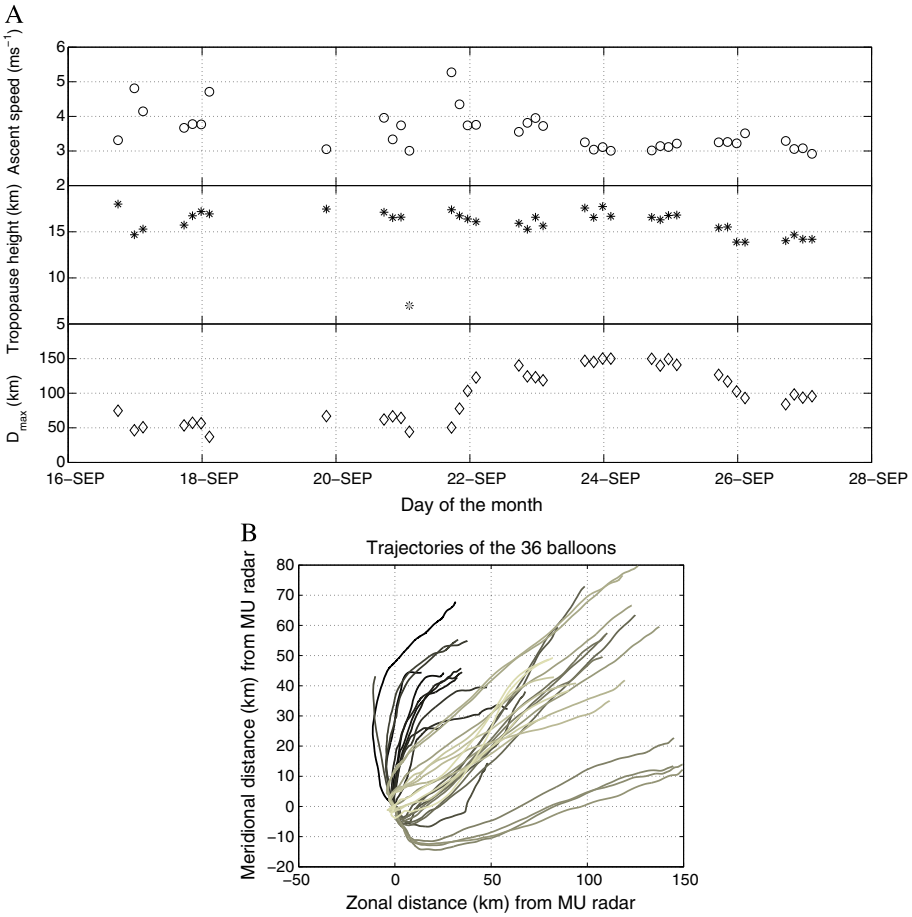

Figure 1. (a) Ascent speed of the 36 balloons (top), tropical tropopause height (middle) and the horizontal distance of the balloon from MUR at the tropopause height (bottom) versus launching time. The light gray star shows the maximum height of reception of the data (balloon 21), not the tropopause height. (b) Balloon trajectories in the horizontal plane for the 36 flights used in the present work. Black: First flight. Lightest gray: Last flight.

maximum distance D_{max} for the data used in the present study (bottom panel). The mean ascent speed was from 5.3 m s^{-1} down to 2.9 m s^{-1} because the balloons were significantly underinflated after 22 September. The tropical tropopause height defined from the temperature profiles ranged between ~14 km and 18 km.

Before 21 September 2011, summer anticyclonic conditions with weak tropospheric winds, positive temperature anomaly, and high relative humidity were met over Japan. On 21 September 2011, typhoon *n*°15 (Roke) passed over Japan close to the radar site during daytime. Just after its passage, the tropospheric jet stream, initially running at higher latitudes, drifted southward. Autumnal weather conditions started from 22 September with negative temperature anomaly at tropospheric heights and the passage of several upper level frontal zones over Japan.

Figure 1b shows the horizontal trajectories of the balloons up to the tropical tropopause height. As shown in the bottom panel of Figure 1a, D_{max} did not exceed 150 km toward North-East and did not exceed ~70 km during the summer conditions before 21 September 2011. Such balloon drifts are not extremely large—these values are quite usual at midlatitudes—but they can be a serious drawback for our purpose. As already discussed in section 1, it must be assumed that the statistical (spectral) properties of the turbulent irregularities measured by the radiosondes are consistent with those detected by the radar at the Bragg scale over horizontal distances of the order of 10^1–10^2 km for quantitative comparisons. The relevance of this hypothesis should strongly depend on the nature of the instabilities generating turbulence. It might be reasonable for turbulence in the sheared regions of synoptic scale fronts so that the source of turbulence detected by radar and balloon can be the same, but surely not, for example, at the top of fair weather cumuli

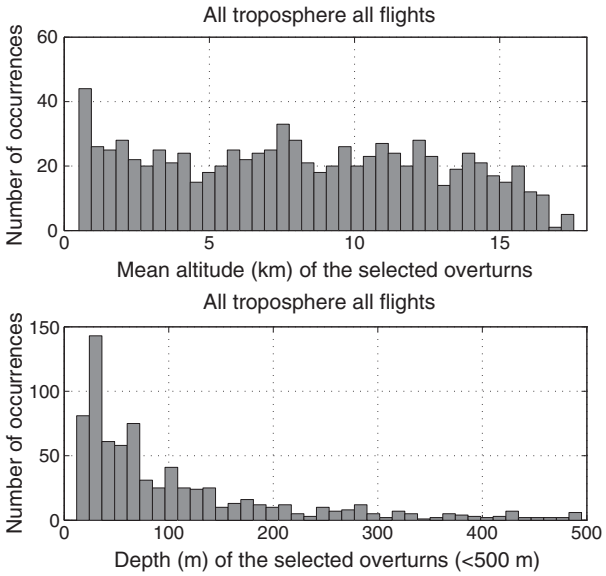

Figure 2. (top) Distribution of the mean height of the selected layers for the 36 soundings. (bottom) The corresponding distribution of overturn depth (<500 m). Of the selected layers, 10.2% exceeded 500 m.

for which turbulence is generated by cloud top entrainment at the aerologic scale (~1.0 km). Consequently, horizontal inhomogeneity can be an important source of errors when performing comparisons. In addition, instabilities associated with inertia-gravity waves, for example, should closely follow tilted isentropic surfaces. Therefore, even though thin layers of turbulence are detected by both instruments, these layers would be observed at different altitudes, possibly resulting in significant errors when comparing radar and balloon data.

3.2. Depth and Mean Altitude of the Selected Turbulent Layers

For the 36 soundings, a total of 854 overturns were ascribed to atmospheric turbulent layers with the criteria described in sections 2.1.1 and 2.1.2 and used by W13, and 886 were attributed to noise. Fifty-five selected layers were found below the first altitude sampled by MUR and, thus, were not used when comparing with radar data. Among the 854 layers, 235 (27.5%) were found in saturated air and 619 (72.5%) in dry air.

Figure 2 (top) reveals a relatively homogeneous frequency distribution of the mean altitude of the 854 selected layers up to the altitude of 13 km. The decreasing distribution beyond this altitude is likely not significant because it is partly due to the variations of the tropopause height (Figure 1a). The peak of distribution near the ground (384 m asl) may reasonably be ascribed to turbulence in the planetary boundary layer. Figure 2 (bottom) shows the corresponding frequency distribution of the depth. The minimum and maximum values are 12 m and 6579 m, respectively. The largest values are related to the presence of clouds extending throughout the troposphere. The distribution has a narrow peak around 30–40 m. However, the low occurrence of overturns at smaller size is likely an artifact due to limitations in resolution. The mean and median values are 222.5 m and 81.0 m, respectively. 33.3% (57.7%) of the selected layers are thinner than 50 m (100 m) and 10.2% are deeper than 500 m. The selected layers fill 34.2% of the total depth of the troposphere. In addition, 84.5% (96.0%) of the rejected layers are thinner than 50 m (100 m).

3.3. Examples of Comparisons

An example of time-height cross section of radar echo power corrected for the range attenuation effects, i.e., $P_V \times r^2$, hereafter noted Pr_V for brevity, for the vertical beam after doing the Capon imaging in the height range 1.245–15 km from 17 September 2011 at 17:00 LT to 18 September 2011 at 04:00 LT is shown in Figure 3. Four balloons were launched at 17:34 LT, 20:35 LT, 23:41 LT, and 02:38 LT. The radar echoes exhibit a complex pattern with more or less long-lived multilayer echoing structures. Rounded echoes of shorter span of time, likely related to convective dynamics, can be noted around 18:50 LT and 02:00 LT. The solid and dashed black curves show the time where the air parcels passed closest to the radar, as explained in section 2.2.2.

Figures 4a–4c show vertical profiles of Pr_V (dB) and Pr_{North} (dB) (black and gray curves, respectively). Results from the east direction are similar to those obtained from the north direction. They are not shown for brevity and clarity of the figures even if azimuth dependence is sometimes not negligible, e.g., *Worthington et al.* [1999]. The superscript of the symbols refers to time averaging. The left panel shows 60 min averaged profiles of Pr_V^{60} and Pr_{North}^{60}, during the balloon flights, and the middle panel shows 10 min averaged profiles of Pr_V^{10} and Pr_{North}^{10} around the instants described by the thick line in Figure 3 for soundings 10–13. The 10 min and 60 min averaged profiles do not show significant differences but, as expected, the 60 min averaged profiles appear to be smoother than the 10 min averaged profiles especially above the altitude of 9.0 km in Figure 4a and

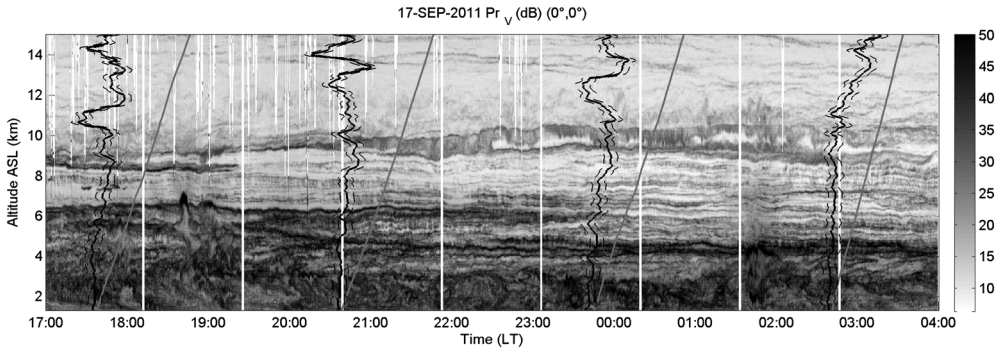

Figure 3. Time-height cross section of MUR echo power (dB) corrected for the range effects (i.e., Pr_V) for 11 h around launching time of balloons 10 to 13 (corresponding to balloons 4 to 7 in Figure 1). The height of the balloons versus time is given by the (slanted) thick gray curves. The curves in thick solid line indicate the instants versus height when air parcels passed closest to the vertical of the radar. The thin dashed lines represent the time interval (here, 10 min) used for time averaging.

logically reveals a larger time variability, as indicated by the standard deviations (shown by horizontal lines). Aspect ratio profiles $AR^{60} = Pr_v^{60}/Pr_{North}^{60}$ (dB) and $AR^{10} = Pr_V^{10}/Pr_{North}^{10}$ (dB) are given in dotted lines. In the Figure 4a (right), pale gray vertical rectangles indicate the altitude range of the selected layers and their corresponding Thorpe lengths.

The main features revealed by Figures 4a–4c are as follows:

1. In Figures 4a and 4b, the selected layers are generally associated with both *maxima* of echo powers and *weak* aspect ratios (i.e., AR^{60} and AR^{10} ~0 dB), as stressed by a black circle on the left panels of the figures. This is the case in Figure 4a for the layers of ~280 m, 440 m, and 480 m in depth at the altitudes of 6.7 km, 7.3 km, and 8.6 km, respectively. These coincidences occur when the horizontal distance between the radar and the balloon is about 20–40 km. This is also the case in Figure 4b at the altitudes of 1.8 km where the selected layer depth is ~160 m, 2.2 km for profiles Pr^{10} (~100 m), 6.5 km (~230 m in total), 7.0 km (~190 m), and in the range 9.7–11.0 km (~1300 m in total). The balloon drifted up to ~60 km at the altitude of 11.0 km. The depths of these turbulent layers are qualitatively consistent with the vertical extent of the radar echo power peaks. Several consecutive overturns should constitute a single turbulent layer around 6.5 km and in the range 9.7–11.0 km in Figure 4b. On the contrary, some of the deepest layers, also associated with *weak* aspect ratios, are associated with *minima* of echo power: in Figure 4a, around 13.8 km (for Pr^{10}) and in Figure 4c at the altitudes of 6.1 km and 16.0 km, and around 11.5 km where several consecutive thin overturns are detected (they are indicated by "asterisks").

   Given that the horizontal distance between the radar and the balloons is a rough estimate of the horizontal extent of the turbulent layers detected by both instruments (ignoring wind advection effects), turbulent layers of 10^2–10^3 m in depth can extend over 10^1–10^2 km along the horizontal. The ratio of depth to horizontal extent can then be 100 typically or more, consistent with other observations [e.g., *Vinnichenko et al.*, 1980]. In Figure 4b, two thin turbulent layers within the range 12.3–12.5 km (also indicated by "asterisks") are associated with a maximum of echo in the profiles of Pr_V^{10} and Pr_{North}^{10} and a minimum in the profiles of Pr_V^{60} and Pr_{North}^{60}. This case illustrates the limits of such a deterministic comparison.

2. On the other hand, turbulent layers are not detected in altitude ranges with strong aspect sensitivity or, if any, they are very thin. Approximately, in Figure 4a, in the altitude range 9–13 km; in Figure 4b, 4.3–6.1 km, 7.0–9.0 km, and 12.5–14.5 km; and in Figure 4c, 2.8–5.5 km, 7.0–11.0 km, and 11.5–16.0 km. The altitude ranges of significant aspect sensitivity are delineated by the vertical gray rectangles in Figures 4a–4c. The only deep turbulent layers associated with significant radar aspect sensitivity are below the altitudes of 6.0 km in Figure 4a and around 7.8 km in Figure 4b where $AR^{10} \approx 5$ to 10 dB (they are indicated by "crosses").
3. Some thin turbulent layers are found near the edges of narrow echo power maxima: in Figure 4a, at the altitudes of 1.7 km and 3.0 km and in Figure 4b, at the altitudes of 2.8, 3.2 km and 4.2 km. (they are indicated by "open diamonds").

The attempt of classification given by (1), (2), and (3) indicates that the detected turbulent layers from balloon measurements do not always correspond to the maxima of radar echo power. Besides the fact that

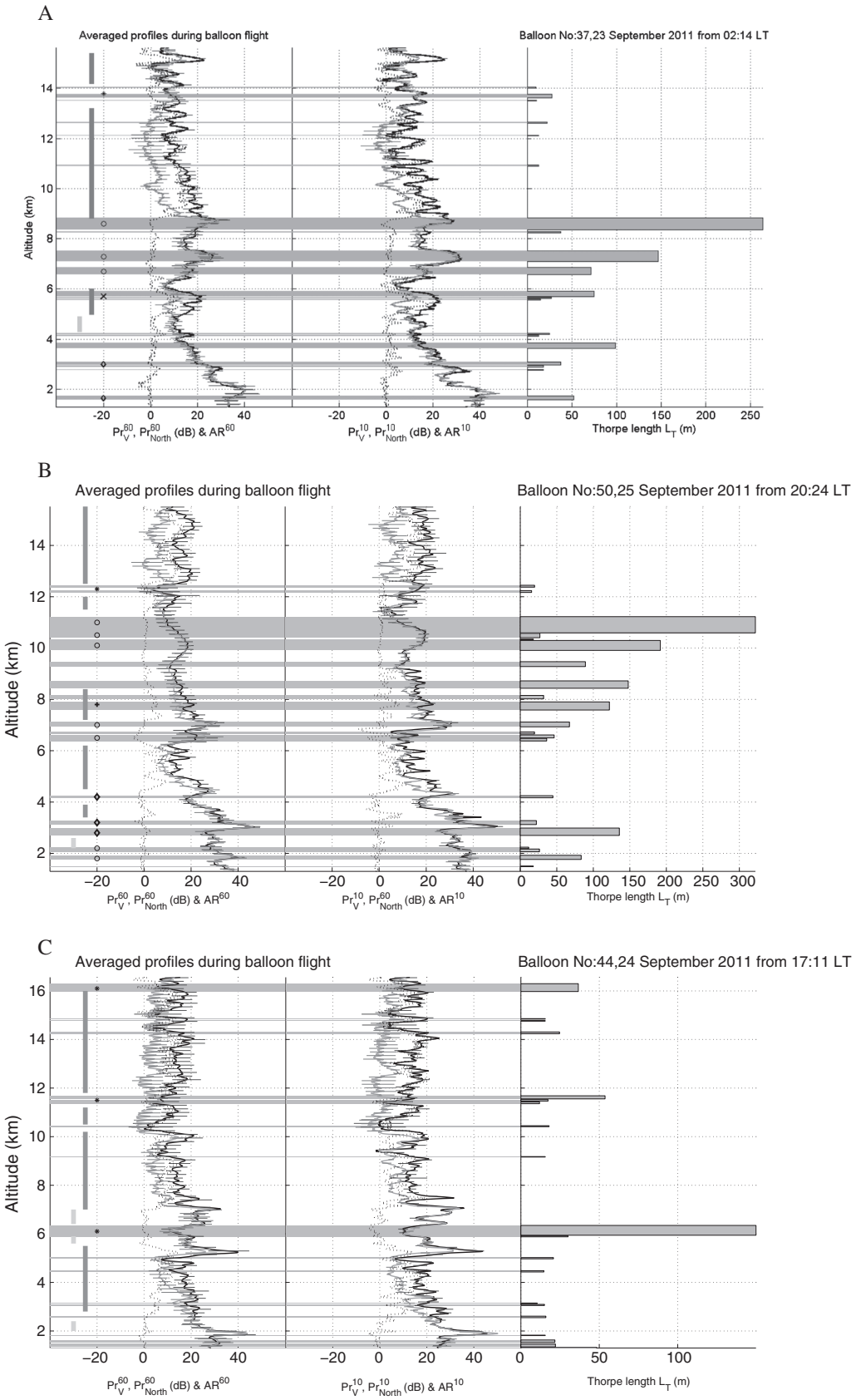

Figure 4

observations are not collocated, it should be noted that the radar echo power depends on the local stratification (through M^2) and that the in situ detected layers may occur within weakly stratified regions. We thus need to further compare quantitatively the refractivity turbulence intensity inferred from both observations. On the other hand, nearly isotropic radar echoes which are not associated with detected layers from the in situ profiles can be noted, in Figure 4a, around 4.5 km, for example. Other cases are found in Figure 4b, around 2.5 km and in Figure 4c, in the ranges 2.0–2.4 km, 5.6–5.9 km, and 6.4–7.0 km even if this selection is slightly subjective since it depends on the time averaging. This nondetection is likely indicative of the limit of comparisons from case studies.

The remaining selected layers are difficult to categorize due to the absence of clear signature in the radar echoes. For the thinnest regions, say ~<50–100 m, as those reported in Figure 4c, the quality of the correspondences is very difficult to evaluate for the reasons discussed in section 2.1.2. The differences between the altitudes of the selected layers and radar peaks with weak aspect ratios noted in Figure 4c could be due to layer tilts, but this assertion, even if plausible due to some apparent slanted echo layers in the echo power images (Figure 3), is rather speculative.

However, as a whole, the correspondences are relatively meaningful, keeping in mind the high vertical resolutions of the radar and balloon data and the (variable) horizontal distance between both kinds of measurements. Any additional interpretation of the results for individual case would likely be subjective. Consequently, the results will now be described in a statistical sense.

3.4. Statistical Analyses

3.4.1. Radar Aspect Ratio in the Selected Layers

The selected cases in Figures 4a–4c showed that the radar echoes are often weakly aspect sensitive in the range of the selected layers. This is confirmed from a statistical study. Figure 5a (top) shows an asymmetric distribution of AR^{10} around ~0 dB. This asymmetry is obviously due to aspect sensitivity in some ranges of the troposphere (see examples in Figures 4a–4c). Similar distributions are obtained for different averaging times (not shown). Figure 5a (bottom) shows the frequency distribution of AR^{10} in the selected layers. It clearly confirms the observations described in section 3.3, i.e., the distribution is very narrow and is nearly symmetric around ~0 dB and follows a lognormal distribution, except around the distribution tails. Weak values of $|AR^{10}|$ are consistent with the dominant mechanism of radar backscattering from isotropic turbulence, and a fortiori with the turbulent nature of the selected layers in a statistical sense. Table 1 indicates quantitative results for radar time averaging of 10 min and 60 min.

Aspect-sensitive radar echoes, as those emphasized by the vertical and narrow gray rectangles in Figures 4a–4c, do not generally coincide with the selected turbulent layers: Aspect ratios >5 dB are found in ~5–7% of the selected layers only (Table 1). Because anisotropic turbulence would produce overturns in the same way as isotropic turbulence in potential temperature profiles, this observation provides further argument in favor of partial reflection from stable gradient sheets for explaining aspect sensitivity. Nonetheless, if anisotropic turbulence remains the main cause of aspect sensitivity, it must occur in thinner layers, not detected because of processing method limitations due to balloon data resolution and instrumental noise effects.

Figure 5b shows aspect ratios AR^{10} as a function of the layer depth up to 500 m for legibility of the figure. The distribution is centered around 0 dB, but large values of AR^{10} are clearly observed for layers thinner than ~100 m. Of the selected layers, 83.4% is associated with $AR^{10} > 5$ dB (i.e., 114 among 140) are thinner than 100 m. Even though anisotropic turbulence at the Bragg scale might be more easily met in thin layers due to a stronger sensitivity to the background stability, it is more likely that differences in the altitudes and/or the

Figure 4. (a) (left) Vertical profiles of Pr_v^{60} (black line), Pr_{North}^{60} (gray line), and AR^{60} (dotted black line) up to the thermal tropopause averaged during the flight of balloon 37 (i.e., flight 20 in Figure 1). The superscript indicates the averaging time (here, 60 min). The solid bars indicate the standard deviation every 150 m (not every 5 m, for legibility of the figure) during the averaging time. The symbols and rectangles in the left panels are described in the text. (middle) The corresponding profiles for an averaging time of 10 min, selecting the instants when the air masses were the closest to the radar (as shown in Figure 3). (right) Range and depth of the selected layers (pale gray vertical rectangles extending in the left and middle panels). The length of the rectangles shows the corresponding Thorpe length. (b) Same as Figure 4a for balloon 50 (flight 30 in Figure 1). (c) Same as Figure 4a for balloon 44 (flight 24 in Figure 1).

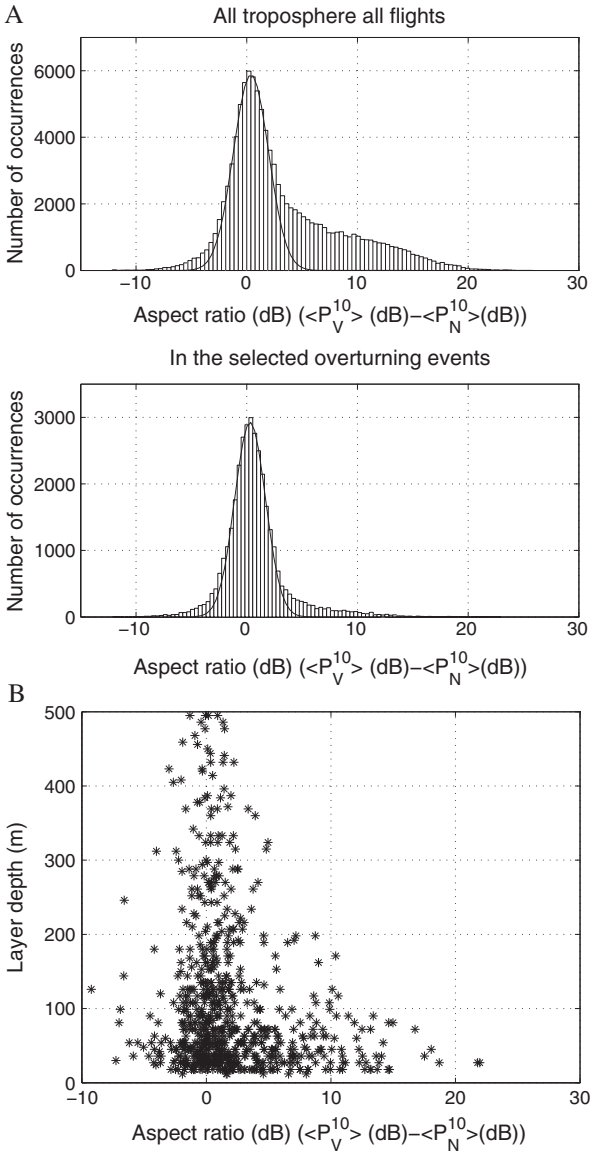

Figure 5. (a) Frequency distributions of radar aspect ratio AR^{10} for the 36 soundings: (top) All the troposphere and (bottom) in the selected layers. Gaussian fits were applied to aspect ratios between −2 dB and +2 dB, and the results are shown by the black curves. (b) Mean radar aspect ratio AR^{10} versus depth of the selected layers.

Table 1. Percentage of High Aspect Ratios (i.e., Arbitrarily, Stronger Than 5 dB) and Weak Aspect Ratios (i.e., Arbitrarily, Weaker Than 3 dB) in the Troposphere (Column 2) and in the Altitude Range of the Selected Layers (Column 3) for Averaging Times of 10 min and 60 min

Aspect Ratio AR (dB)	All (%)	In the Selected Layers (%)
$AR^{10} > 5$	28.8	6.8
$\|AR^{10}\| < 3$	57.4	83.2
$AR^{60} > 5$	27.8	4.9
$\|AR^{60}\| < 3$	60.4	88.6

limited horizontal extent and life span of the thin layers are the cause of this observation. Consequently, comparisons may not be relevant for most thin layers and additional statistical results will also be shown after rejecting layers thinner than 100 m.

3.4.2. Temperature and Refractivity Constant Structures

Figure 6 displays all the values of (dry) squared Brunt-Vaïsälä frequency $N_d^2 = g/\theta\, d\theta/dz$ (in $\log_{10}$ scale) (a), C_T^2 (b), dry C_n^2 (c), and moist C_n^2 (d) in dB versus height estimated from balloon data in the selected layers using relations (2) to (4). A third-order polynomial fit has been applied to each distribution (gray curve). The distribution of N_d^2 is shown in order to interpret the dependence of C_T^2 with height. Indeed, C_T^2 does not significantly vary with height up to the altitude of 12.0 km but increases above this altitude (Figure 6b). It is clearly related to the increase of the background stability N^2 (Figure 6a). Dry C_n^2 shows a slow decrease of -1 dB km^{-1} up to 12 km which can be strictly explained by the decrease of air density with height (Figure 6c). The distribution of moist C_n^2 is much more scattered than C_T^2 and shows a higher dependence with height up to ~13 km (Figure 6d). The polynomial fit decreases at a rate of ~-2.5 dB km^{-1}. *Naström et al.* [1986] reported a similar trend (decrease ≤ -2 dB km^{-1}) in the troposphere from monthly averaged profiles of C_n^2 measured with the Poker Flat and Flatville VHF radars. *Naström and Eaton* [1997] showed a decrease of -3.5 dB km^{-1} for seasonal profiles from measurements with the 50 MHz White Sand Missile Range radar. As discussed by these authors and others, C_n^2 in the troposphere is dominated by the humidity contribution, which decreases with height and is strongly variable.

3.4.3. Comparisons Between Moist C_n^2 and Radar Echo Power

Direct comparisons between moist C_n^2 estimated in the selected layers and radar echo power in the same altitude ranges can be justified for the following reasons:

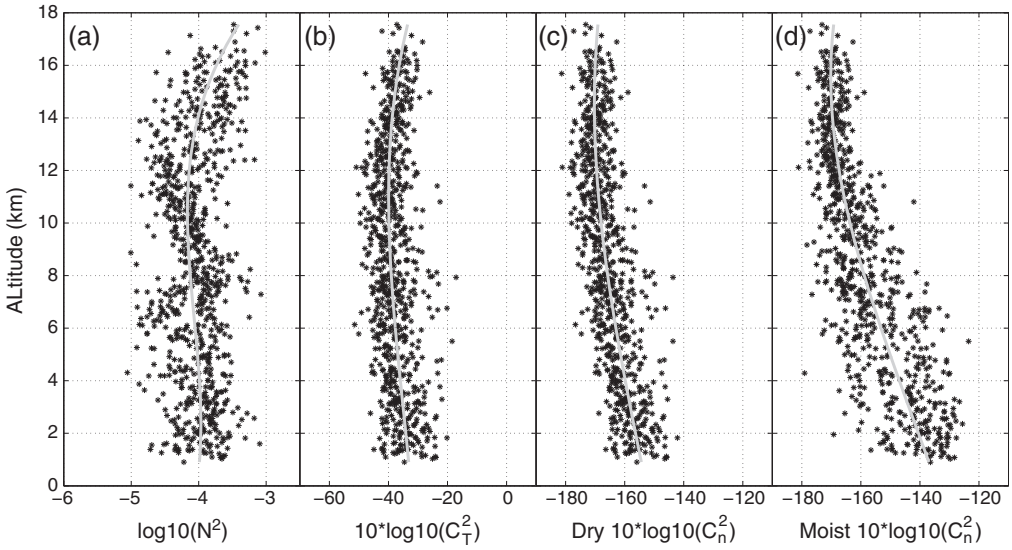

Figure 6. (a) The $\log_{10}(N^2)$ estimated from the measured potential temperature profiles in the range of the selected layers for 36 soundings. (b) The corresponding values of C_T^2 (in dB scale), (c) dry C_n^2 (dB), and (d) moist C_n^2 (dB). The solid gray lines indicate the result of third-degree polynomial fits.

1. If the radar is sensitive to Kolmogorov turbulence in an inertial subrange, the relationship between the radar echo power P and C_n^2 is given by

$$C_n^2 = K\ P\ \times\ r^2 \tag{9}$$

where K is a function of the radar operating system parameters. Since K is not established for MUR, the comparisons will be made in relative levels.

2. From a statistical point of view, the radar echoes associated with the selected layers are not aspect sensitive (Figure 5a). This is a necessary condition, consistent with the mechanism of backscattering from isotropic turbulence.
3. The knowledge of the fraction of the radar volume which is turbulent (discussed by, e.g., *Van Zandt et al.* [1978]) is less a problem here because the range resolution is greatly improved by the range-imaging technique despite the finite radar beam width (two-way half-power half beam width = 1.32°). This is a crucial advantage with respect to previous studies based on radar data at a coarser range resolution.

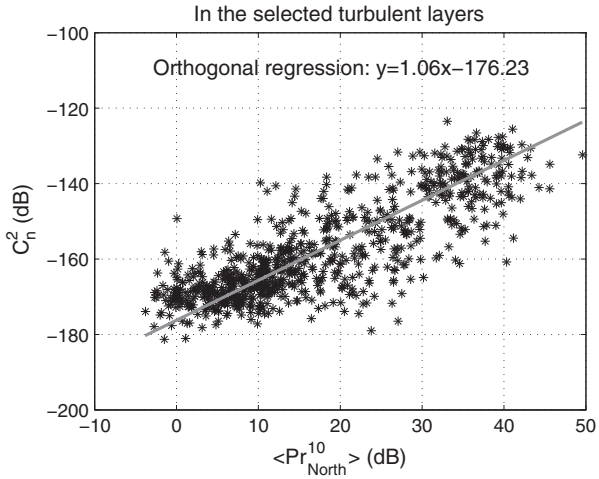

Figure 7. Pr_{North}^{10} versus moist C_n^2 (dB) (shown in Figure 6d). The solid gray line is the result of a linear fitting using an orthogonal regression.

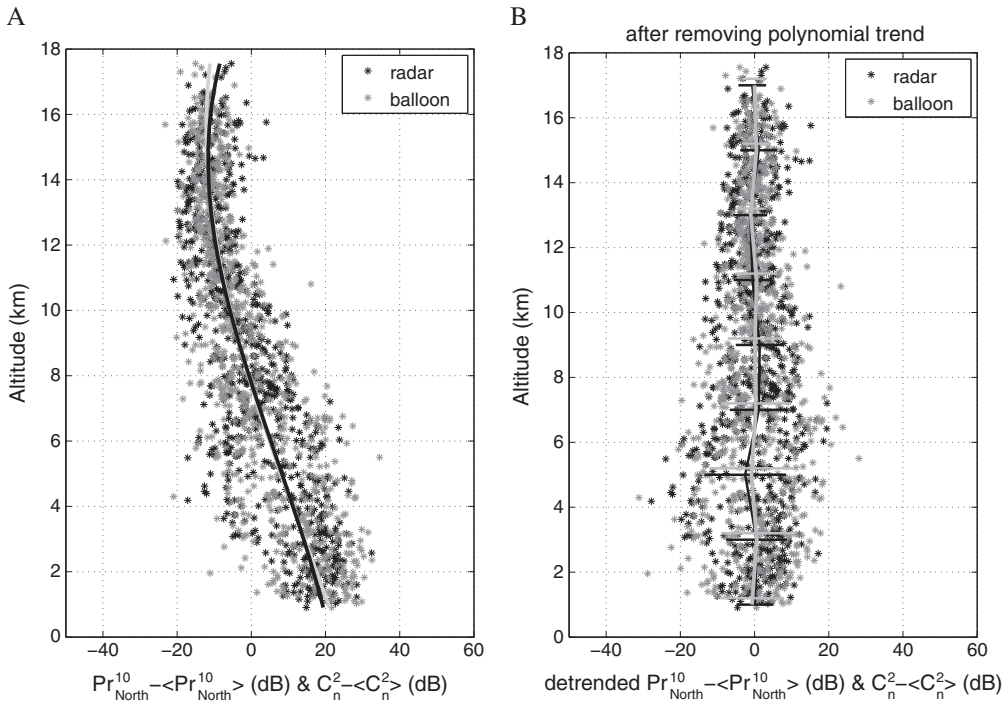

Figure 8. (a) $C_n^2 - \langle C_n^2 \rangle$ (dB) and $Pr^{10}_{North} - \langle Pr^{10}_{North} \rangle$ (dB) versus altitude. The thick black and light gray curves are the result of a fitting with a polynomial of degree 3. (b) Same as Figure 8a after removing the polynomial trend. Black and light gray lines are the mean profiles and twice the standard deviation values over segments of 2 km from 0 km.

On the basis of items 1–3 above, direct comparisons between C_n^2 estimated from balloon data and radar echo power taken with either the vertically or obliquely directed antenna can be made.

Figure 7 shows the scatterplot of radar echo power Pr^{10}_{North} versus moist C_n^2 estimated from expressions (4)–(6). Nine aberrant values of C_n^2 have been rejected (they do not appear in Figure 6d). The scatterplot shows a large spread (over 40 dB), but both statistics show similar dynamics (of about 50 dB). The slope of the curve obtained from a linear regression is ~1.06 (i.e., close to 1) indicating that the radar echo power corrected for the range attenuation effects is indeed statistically proportional to C_n^2 (expression (9)). This result gives credence to the interpretation of the radar echoes in terms of pure turbulent scattering. It also upholds the interpretation of the selected layers from balloon data in terms of turbulent layers. The large spread of the scatterplot suggests, however, that these conclusions are only relevant in a statistical sense and are not representative of each selected layer independently for all the aforementioned—practical and conceptual—reasons.

The scatterplots versus height of $C_n^2(\mathrm{d}B) - \langle C_n^2(\mathrm{d}B) \rangle$ and $Pr^{10}_{North}(\mathrm{d}B) - \langle Pr^{10}_{North}(\mathrm{d}B) \rangle$ are shown in Figure 8a. As with the distribution of C_n^2, a third-degree polynomial fitting was also applied to the distribution of Pr^{10}_{North} (black curve). The two polynomial trends are almost identical (except a difference of a few dB below ~2 km and above 16 km) in accordance with the linear relationship between the two statistics shown in Figure 7. The scatter of C_n^2 (dB) versus height is very similar to the scatter observed for Pr^{10}_{North} (dB). A maximum of scatter is found in the height range of 4.0–6.0 km as quantified by twice the standard deviations in Figure 8b. It slowly decreases above the altitude of 6.0 km, very likely due to decreasing water vapor content. Below 3.0 km, the height variations of relative humidity, often close to saturation were smaller than above (not shown), consistent with smaller scatter. Figure 8b shows the distributions versus height of the detrended distributions of C_n^2 and Pr^{10}_{North}. The values averaged over segments of 2.0 km are close to 0 dB, indicating that the polynomial detrend correctly removed the systematic height variations of both statistics.

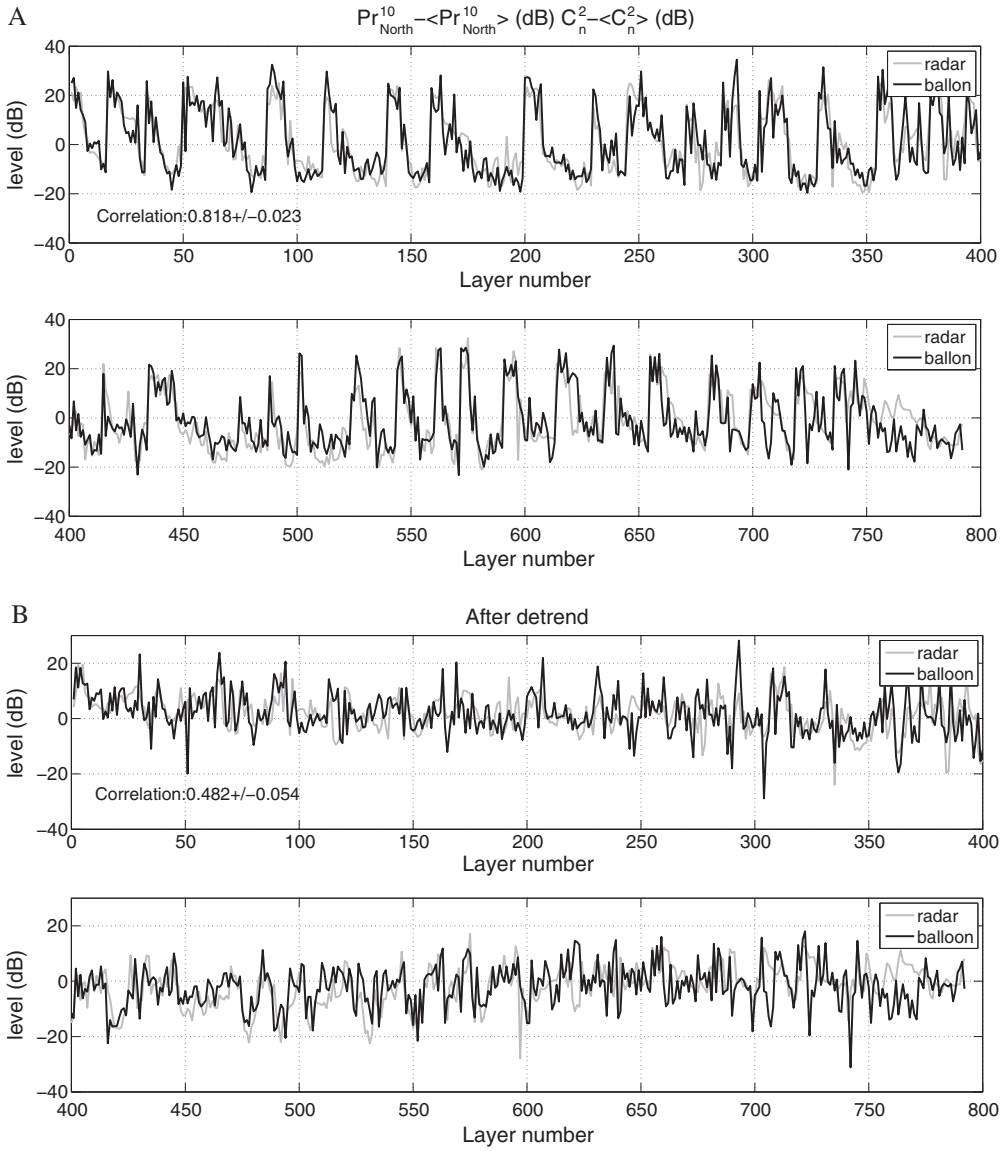

Figure 9. (a) Comparison of $C_n^2 - \langle C_n^2 \rangle$ and $Pr^{10}_{North} - \langle Pr^{10}_{North} \rangle$. The correlation of the two series is given with an interval confidence of 95%. (b) Same as Figure 9a but after the polynomial detrend in order to remove the main tendency.

Figure 9a takes together all the estimates of $C_n^2 - \langle C_n^2 \rangle$ and $Pr^{10}_{North} - \langle Pr^{10}_{North} \rangle$ (i.e., 799) for the 36 balloons in consecutive and chronological orders. The plots are divided into two panels for legibility. The sawtooth shape of the plots results from the systematic decreasing tendency with height. The cross-correlation coefficient is ~0.818 with a 95% interval confidence of ±0.023. The fact that the dynamics of both signals is nearly identical gives us extra credence that the quantities are effectively related.

However, such a high correlation is mainly due to the systematic decrease and large dynamics (~40 dB) of C_n^2 and Pr^{10}_{North} with height. Therefore, it is not representative of the quality of the model to reconstruct the specific events occurring in each profile. For this, the use of the detrended profiles (Figure 9b) is required. A cross-correlation coefficient of ~0.482 ± 0.054 is found. It corresponds to the "degree of resemblance" between the radar- and balloon-derived values deviating from the "general trend" given by the polynomial fit.

Cross-correlation coefficients using the original and detrended profiles (1) for radar time averages over 2, 10, 30, and 60 min, (2) when using vertical and oblique radar beams, (3) for all the selected layers, and

Table 2. Cross-Correlation Coefficients Between C_n^2 and Pr for Different Averaging Times, When Using the Vertical and Northward Beams, for All Selected Layers With and Without Polynomial Detrend and for Layers Deeper Than 100 m

Integration Time (min)	Radar Beam	All Layers No Detrend	Depth >100 m No Detrend	All Layers With Detrend	Depth >100 m With Detrend
2	V	0.776	0.839	0.384	0.441
	N	0.795	0.835	0.449	0.470
10	V	0.793	0.853	0.410	0.480
	N	0.818	0.861	0.482	0.516
30	V	0.812	0.867	0.444	0.517
	N	0.829	0.876	0.498	0.549
60	V	0.826/0.834[a]	0.875/0.878[a]	0.473/0.492[a]	0.533/0.540[a]
	N	0.838/0.844[a]	0.881/0.881[a]	0.516/0.531[a]	0.561/0.558[a]

[a]For 60 min, the cross-correlation coefficients are also given when selecting radar profiles during the balloon flight from the launch time.

(4) for layers deeper than 100 m are listed in Table 2 (for legibility, the interval confidences are not given). We show the following:

1. The cross-correlation coefficients are generally very slightly better when using the northward beam likely due to a residual, but not totally negligible, effect of aspect sensitivity when using the data collected from vertical beam.
2. The cross-correlation coefficients slightly increase with time averaging of the radar profiles by ~0.05 between 2 and 60 min. Indeed, longer time averaging should produce more statistically representative radar profiles.
3. The cross-correlation coefficients also increase by ~0.05 and exceed 0.88 when selecting the layers deeper than 100 m. This improvement may mainly be ascribed to the large horizontal extent and life span of these layers compared to thinner layers as discussed in section 3.4.1.
4. The cross-correlation coefficients obtained from radar profiles averaged from the start of the balloon flights are equivalent to those obtained when wind advection is taken into account. This result contradicts a similar analysis made by *Luce et al.* [2007] who emphasized the importance to take account for wind advection when comparing N^2 estimates at a vertical resolution of 50 m from balloon and MUR data at stratospheric heights (e.g., their Figure A2). In the present case, it appears that the main features of radar echo power during the balloon flights were not very different from those observed at the instants when air parcels passed closest to the vertical of the radar. In summary, Table 2 shows that the radar integration time, the direction of radar beam, and the advection by the wind are not crucial parameters for such comparisons.

In order to better understand the significance of the estimated cross-correlation coefficients, we performed tests consisting of rearranging randomly the order of the 36 soundings. For this purpose, 20 realizations were made. The correlation coefficients are ~0.61–0.67 without detrend (not shown). These high values can be explained by the systematic decrease of C_n^2 with height. Nevertheless, it is significantly smaller than the normal values (~0.77–0.88). The fact that the dynamics of both balloon C_n^2 and radar echo power are similar offers a mean to calibrate radar measurements of refractivity on balloon estimates. After detrending, the correlation coefficient is ~0 (not shown). We thus suitably removed the contributions of the "universal" decrease of C_n^2 with height. Cross-correlation coefficients of ~0.38–0.56 from detrended profiles are thus significant values and demonstrate that our statistics are also representative of the specific turbulent events detected during each sounding.

4. Summary and Conclusions

The present work aimed to demonstrate the relevance of recently developed radar and balloon data processing techniques for studying turbulence in the troposphere. First, processing methods based on Thorpe sorting and optimized by *Wilson et al.* [2010, 2011] were applied to dry and moist potential temperature profiles estimated from radiosonde data for detecting overturns presumably produced by turbulence. Second, concurrent measurements with a VHF band radar (MUR) in range-imaging mode were performed for detecting and monitoring turbulent events in great detail [e.g., *Luce et al.*, 2006]. Comparisons

were made from a data set of 36 soundings collected at night during a measurement campaign in September 2011 at the Shigaraki MU observatory (Japan).

A first issue was whether the processed radar and balloon data identified at some occasions the same turbulent events in the same height ranges. It was found that the deepest layers (typically >100 m in depth) selected from balloon data very often showed clear signatures in the radar echo power profiles. The horizontal drift of the balloons (typically a few tens of kilometers) suggests that the horizontal extent of most turbulent layers of a few hundreds of meters in depth should exceed several tens of kilometers (i.e., about 100 times the layer depth). Isotropic peaks of echo power were very frequently observed in the height range of the turbulent layers identified from balloon data. This is the most expected contribution of turbulence to the radar echoes. In contrast, some events were associated with (relative) minima of echo power but still isotropic. Even if the different stages of turbulence for a single event could not be identified from our data set, this observation may reveal a later stage of turbulence (homogenization due to turbulent mixing). This characteristic may support the widespread idea that echo power is not always representative of the dynamic turbulence but should be more surely quantified by spectral width of Doppler spectra [e.g., *Hooper and Thomas*, 1998; *Fritts et al*., 2011]. Finally, turbulent layers were very rarely found in the height ranges of zenith aspect-sensitive (vertically enhanced) radar echoes. This result indicates that a radar backscatter mechanism like partial reflection from gradient sheets is more likely to explain the vertically enhanced radar echoes than scattering from anisotropic turbulence [*Röttger and Liu*, 1978; *Hooper and Thomas*, 1998].

Another issue was to study the relevance of models for retrieving statistics that quantify the intensity of turbulence from radar and balloon data. First, a theoretical basis for estimating the temperature structure constant C_T^2 from temperature variance and Thorpe length was proposed (expression (5)). Then, C_T^2 estimated for each selected layer was converted into the refractive index structure constant C_n^2 by including humidity contribution from expression (6). The C_n^2 values thus obtained were compared with the radar echo power values corrected for range attenuation effects averaged in the height range of the selected layers. Several comparisons were performed by applying various integration times of the radar data (from 2 to 60 min) during the balloon flights, by taking account for the advection of the air parcels by the horizontal wind and by considering the layers deeper than 100 m only. The two statistics were found to be proportional for all comparisons and high correlation coefficients (0.77–0.88) were obtained. However, these high correlation coefficients hide a wide dispersion of the scatterplot (over about 40 dB), which may explain the weak sensitivity of the results to the comparison method. It was shown that the obtained correlation coefficients were mostly caused by the systematic decrease of C_n^2 with height up to 13 km due to the decrease of humidity and density. Detrended values still showed significant positive correlation coefficients (~0.5) and were representative of the degree of resemblance between the values deviating from the systematic dependence with height of C_n^2. Therefore, by rejecting aspect-sensitive echoes and assuming that all the nonaspect-sensitive echoes result from backscatter from isotropic turbulence, it follows that time-height cross sections of C_n^2 at high resolutions can be obtained from MUR measurements based on the assumption that C_T^2 estimated from balloons are relevant. Further studies already started by *Wilson et al*. [2014] will provide additional insights to the characteristics of turbulent layers identified from concurrent radar and balloon observations (energetics and turbulence length scales).

Appendix A: Ice Saturated Potential Refractive Index Gradient

Vaughan and Worthington [2000] established the expression of the saturated refractive index gradient M_s for saturation vapor pressure over water (their formula (15)). Note that a factor 2 is missing in the third term of the first bracket of their expression. M_s can be obtained for negative temperatures from the empirical expression (7) for the saturation vapor pressure over ice or by using the Clausius-Clapeyron equation for de_i/dT. It follows that

$$M_s \approx -A\frac{p}{T}\left(1+B\frac{r_i}{T}-C\frac{r_i}{T^2}\right)\frac{1}{T}\left(\frac{dT}{dz}+\Gamma_m\right) \tag{A1}$$

where $A = 0.776\times10^{-6}$, B = 15,466.24 and C = 9.502×10^{7}. The parameter r_i is the saturation mixing ratio over ice (g/g), Γ_m is the saturated lapse rate (for negative temperature), p is in Pa and T in Kelvin. If $r_i \to 0$, $\Gamma_s \to \Gamma_a$,

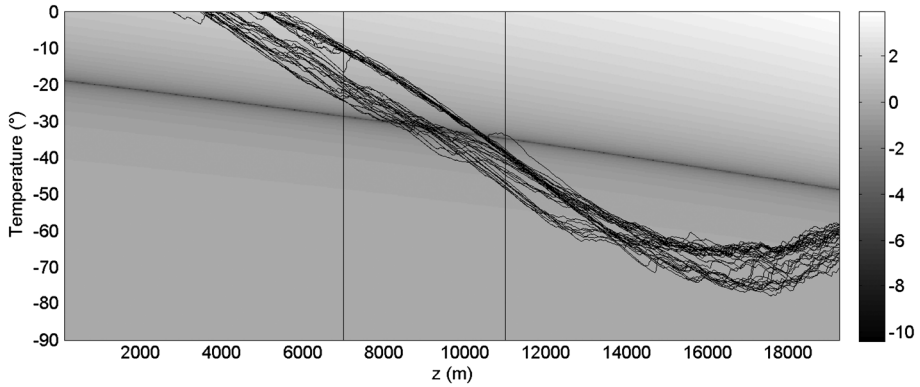

Figure A1. Plot of $20\log_{10}\left(1+B\frac{r_i}{T}-C\frac{r_i}{T^2}\right)$ versus temperature and altitude. The solid curves show the temperature profiles measured during the experiment.

and $M_s \rightarrow M_d$. $M_s = 0$ when the first term in brackets vanishes. Since r_i depends on pressure and temperature, Figure A1 shows $T = 20\log_{10}\left(1+B\frac{r_i}{T}-C\frac{r_i}{T^2}\right)$ for $-80 < T < 0$°C and $50 < p < 1000$ hPa (converted into altitudes assuming a "standard atmosphere"). Superimposed are the temperature profiles obtained during the 36 soundings.

The term T produces small values of M_s (and thus weak echo power if the model is relevant) in the height range 7–11 km. Its contribution is small on both sides of this range for realistic temperatures. Figure A2 shows the results of comparison between $Pr^{10}_{\mathrm{North}}(\mathrm{dB}) - \left\langle Pr^{10}_{\mathrm{North}}(\mathrm{dB})\right\rangle$ and $C_n^2(\mathrm{dB}) - \left\langle C_n^2(\mathrm{dB})\right\rangle$ when replacing M_h by M_s in expression (6) for saturated regions (expression (A1) for negative temperatures and its equivalent expression for positive temperatures). Some values of C_n^2 seem to be underestimated (due to the properties of M_s) by ~10–20 dB in the height range 7–11 km with respect to radar estimates (if we assume that the empirical calibration of MUR is correct).

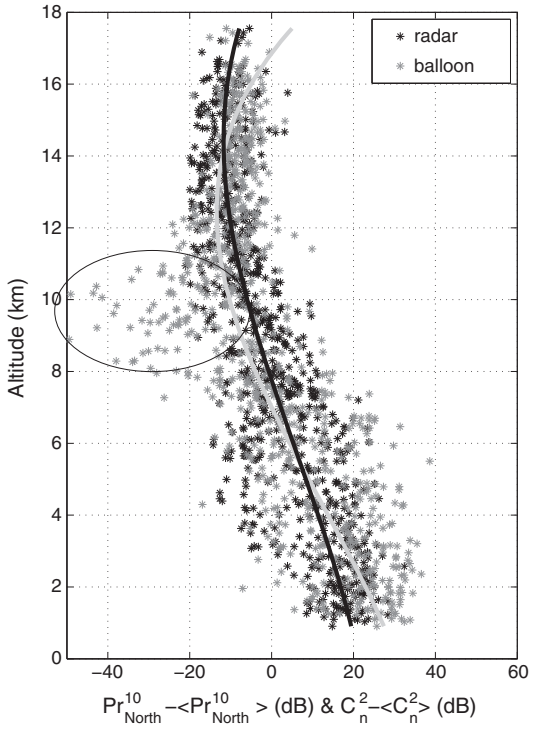

Figure A2. Same as Figure 8a (i.e., $Pr^{10}_{\mathrm{North}}(\mathrm{dB}) - \left\langle Pr^{10}_{\mathrm{North}}(\mathrm{dB})\right\rangle$ and $C_n^2(\mathrm{dB}) - \left\langle C_n^2(\mathrm{dB})\right\rangle$ versus height) when using M_s instead of M_h for saturated layers. The altitude range where it is strongly underestimated is emphasized by the ellipse.

Acknowledgments
Part of this work has been carried out by one of the authors (H. L.) at RISH during a stay funded by the National Institute of Communications and Technology (NICT). MUR belongs to and is operated by RISH. Balloons were funded by LATMOS.

References

Dillon, T. (1982), Vertical overturns: A comparison of Thorpe and Ozmidov scales, *J. Geophys. Res.*, *87*, 9601–9613, doi:10.1029/JC087iC12p09601.
Durran, D., and J. Klemp (1982), On the effects of moisture on the Brunt-Vaïsälä frequency, *J. Atmos. Sci.*, *39*, 2152–2158.
Emanuel, K. A. (1994), *Atmospheric Convection*, 580 pp., Oxford Univ. Press, New York.
Fritts, D. C., P. Franke, K. Wan, T. Lund, and J. Werne (2011), Computation of clear-air radar backscatter from numerical simulations of turbulence, II: Backscatter moments throughout the lifecycle of a Kelvin-Helmholtz instability, *J. Geophys. Res.*, *116*, D11105, doi:10.1029/2010JD014618.
Fukao, S., T. Sato, T. Tsuda, M. Yamamoto, and M. D. Yamanaka (1990), MU radar—New capabilities and system calibrations, *Radio Sci.*, *25*, 477–485, doi:10.1029/RS025i004p00477.
Hooper, D. A., and L. Thomas (1998), Complementary criteria for identifying regions of intense atmospheric turbulence using lower VHF radar, *J. Atmos. Sol. Terr. Phys.*, *60*, 49–61.
Houze, R. A., Jr. (1993), *Cloud Dynamics*, 573 pp., Academic Press, San Diego Calif.
Lalas, D., and F. Einaudi (1974), On the correct use of the wet adiabatic lapse rate in stability criteria of a saturated atmosphere, *J. Appl. Meteorol.*, *13*, 318–324.
Luce, H., M. Crochet, F. Dalaudier, and C. Sidi (1995), Interpretation of VHF ST radar vertical echoes from in situ temperature sheet observations, *Radio Sci.*, *30*, 1002–1025, doi:10.1029/95RS00713.
Luce, H., F. Dalaudier, M. Crochet, and C. Sidi (1996), Direct comparison between in situ and VHF oblique radar measurement of refractive index spectra: A new successful attempt, *Radio Sci.*, *31*, 1487–1500, doi:10.1029/96RS02087.
Luce, H., M. Yamamoto, S. Fukao, D. Hélal, and M. Crochet (2001), A frequency radar interferometric imaging applied with high resolution methods, *J. Atmos. Sol. Terr. Phys.*, *63*, 221–234.
Luce, H., G. Hassenpflug, M. Yamamoto, and S. Fukao (2006), High-resolution vertical imaging of the troposphere and lower stratosphere using the new MU radar system, *Ann. Geophys.*, *24*, 791–804.
Luce, H., G. Hassenpflug, M. Yamamoto, M. Crochet, and S. Fukao (2007), Range-imaging observations of cumulus convection and Kelvin-Helmholtz instabilities with the MU radar, *Radio Sci.*, *42*, RS1005, doi:10.1029/2005RS003439.
May, P. T., M. Yamamoto, S. Fukao, T. Sato, S. Kato, and T. Tsuda (1991), Wind and reflectivity fields around fronts observed with a VHF radar, *Radio Sci.*, *26*, 1245–1249, doi:10.1029/91RS00964.
Nastrom, G. D., and F. D. Eaton (1997), Turbulence eddy dissipation rates from radar observations at 5–20 km at White Sands Missile Range, New Mexico, *J. Geophys. Res.*, *102*, 19,495–19,505, doi:10.1029/97JD01262.
Nastrom, G. D., K. S. Gage, and W. L. Ecklund (1986), Variability of turbulence, 4–20 km, in Colorado and Alaska from MST Radar Observations, *J. Geophys. Res.*, *91*, 6722–6734, doi:10.1029/JD091iD06p06722.
Ottersten, H. (1969), Atmospheric structure and radar backscattering in clear air, *Radio Sci.*, *4*, 1179–1193, doi:10.1029/RS004i012p01179.
Röttger, J. (1980), Reflection and scattering of VHF radar signals from atmospheric refractivity structures, *Radio Sci.*, *15*, 259–276, doi:10.1029/RS015i002p00259.
Röttger, J., and C. H. Liu (1978), Partial reflection and scattering of VHF radar signals from the clear air atmosphere, *Geophys. Res. Lett.*, *5*, 357–360, doi:10.1029/GL005i005p00357.
Smyth, W. D., J. M. Moum, and D. R. Caldwell (2001), The efficiency of mixing in turbulent patches: Inferences from direct simulations and microstructure observations, *J. Phys. Oceanogr.*, *31*, 1969–1992.
Tatarski, I. (1961), *Wave Propagation in a Turbulent Medium*, edited by R. A. Silvermann, McGraw-Hill, New York.
Thorpe, S. A. (1977), Turbulence and mixing in a Scottish Lock, *Philos. Trans. R. Soc. London, Ser. A*, *286*, 125–181.
Tsuda, T., P. T. May, T. Sato, S. Kato, and S. Fukao (1988), Simultaneous observations of reflection echoes and refractive index gradient in the troposphere and lower stratosphere, *Radio Sci.*, *23*, 655–665, doi:10.1029/RS023i004p00655.
Van Zandt, T. E., J. L. Green, K. S. Gage, and W. L. Clark (1978), Vertical profiles of refractivity turbulence structure constant: Comparison of observations by the Sunset radar with a new theoretical model, *Radio Sci.*, *13*, 819–829, doi:10.1029/RS013i005p00819.
Vaughan, G., and R. M. Worthington (2000), Effects of humidity and precipitation on VHF radar vertical beam echoes, *Radio Sci.*, *6*, 1389–1398, doi:10.1029/1999RS002260.
Vinnichenko, N. K., N. Z. Pinus, S. M. Shmeter, and G. N. Shur (1980), *Turbulence in the Free Atmosphere*, 310 pp., Plenum Pub., New York.
Wilson, R., H. Luce, F. Dalaudier, and J. Lefrère (2010), Patch identification in potential density/temperature profiles, *J. Atmos. Oceanic Technol.*, *27*, 977–993, doi:10.1175/2010JTECHA1357.1.
Wilson, R., F. Dalaudier, and H. Luce (2011), Can on detect small-scale turbulence from standard meteoroical radiosondes?, *Atmos. Meas. Tech.*, *4*, 969–1000.
Wilson, R., H. Luce, H. Hashiguchi, and M. Shiotani (2013), On the effect of moisture on the detection of tropospheric turbulence from in situ measurements, *Atmos. Meas. Tech.*, *6*, 697–702.
Wilson, R., H. Luce, H. Hashiguchi, N. Nishi, and Y. Yabuki (2014), Energetics of persistent turbulent layers underneath mid-level clouds estimated from concurrent radar and radiosonde data, *J. Atmos. Sol. Terr. Phys.*, *118*, 78–89, doi:10.1016/j.jastp.2014.01.005.
Worthington, R. M., R. D. Palmer, and S. Fukao (1999), Complete maps of the aspect sensitivity of VHF atmospheric radar echoes, *Ann. Geophys.*, *17*, 1116–1119.
Zhang, J., H. Chen, Z. Li, X. Fan, L. Peng, Y. Yu, and M. Cribb (2010), Analysis of cloud layer structure in Shouxian, China using RS92 radiosonde aided by 95 GHz cloud radar, *J. Geophys. Res.*, *115*, D00K30, doi:10.1029/2010JD014030.